

ARTICLES

Superionic and Superconducting Nanohybrids with Heterostructure, $\text{Ag}_x\text{I}_w\text{Bi}_2\text{Sr}_2\text{Ca}_{n-1}\text{Cu}_n\text{O}_y$ ($0.76 \leq x \leq 1.17$, $n = 1, 2$, and 3)**Jin-Ho Choy,* Young-Il Kim, and Seong-Ju Hwang***Department of Chemistry, Center for Molecular Catalysis, College of Natural Sciences, Seoul National University, Seoul 151-742, Korea**Received: May 28, 1998*

New mixed conducting hybrid systems, $\text{Ag}_x\text{I}_w\text{Bi}_2\text{Sr}_2\text{Ca}_{n-1}\text{Cu}_n\text{O}_y$ ($n = 1, 2$, and 3), have been developed successfully by intercalating the superionic conducting Ag–I layer into the superconducting $\text{Bi}_2\text{Sr}_2\text{Ca}_{n-1}\text{Cu}_n\text{O}_y$ lattice. Although the Ag–I intercalation gives rise to a remarkable basal increment of ~ 7.3 Å, which is twice as large as that of the iodine intercalate ($\Delta d = 3.6$ Å), it has little influence on the superconducting property with only a slight T_c depression. Systematic X-ray absorption near edge structure (XANES)/extended X-ray absorption fine structure (EXAFS) studies clearly reveal the charge transfer between host and guest, indicating that a change in hole concentration of the CuO_2 layer is the main origin of T_c evolution upon intercalation. According to the ac impedance and dc relaxation analyses, the $\text{Ag}_x\text{I}_w\text{Bi}_2\text{Sr}_2\text{Ca}_{n-1}\text{Cu}_n\text{O}_y$ compounds possess fast ionic conductivities ($\sigma_i = 10^{-1.4} - 10^{-2.6} \Omega^{-1} \text{cm}^{-1}$ at 270°C) with the activation energies of 0.22 ± 0.02 eV, which are similar to those of other two-dimensional Ag^+ superionic conductors. A more interesting finding is that these intercalates exhibit both high electronic and ionic conductivities with ionic transference numbers of $t_i = 0.02 - 0.60$, due to their interstratified heterostructures consisting of a superionic conducting silver iodide layer and a metallic host layer. A close relationship between local crystal structure and ionic conductivity has been elucidated from the detailed Ag K -edge EXAFS analyses, where a reasonable pathway for Ag^+ ionic conduction is suggested along with the intracrystalline structure of the Ag–I sublattice.

Introduction

In the field of material science, one of the most fundamental research subjects has been the synthesis of new compounds with unusual physicochemical functions. Among these compounds, the mixed ionic and electronic conductor has attracted much interest because of its wide applicability as an electrode in various electrochemical devices.¹ However, it is very difficult to develop new mixed conducting materials, because they should have both the appropriate crystal structure and electronic band gap favorable for ionic and electronic conduction, respectively.² Such a difficulty would be overcome if it were possible to hybridize an electronic conducting layer with an ionic conducting layer into the same crystal lattice.³ In fact, we have successfully developed such a hybrid system, although not ionically conducting, by intercalating mercuric halides into Bi-Sr-Ca-Cu-O superconductors.^{4,5} On the basis of the same synthetic strategy, we were also successful in synthesizing a new type of mixed ionic and electronic conductor, Ag–I intercalated $\text{Bi}_2\text{Sr}_2\text{CaCu}_2\text{O}_y$, which is an excellent example of tailoring the material property through the intercalation technique.⁶ This new molecular hybrid system provides opportunities not only to explore the effect of basal increment on the high- T_c superconductivity but also to study the ionic conducting behavior of the Ag–I species stabilized in the interlayer space

of a two-dimensional oxide lattice. Furthermore, it has been found that the content of guest silver iodide can be controlled by adjusting the initial mixing ratio of silver metal and the pristine compound, at the synthetic step, which allows us to freely tune both the concentrations of electronic and ionic charge carriers. In this context, we have extended our research to the entire solid solution of the $\text{Ag}_x\text{I}_w\text{Bi}_2\text{Sr}_2\text{Ca}_{n-1}\text{Cu}_n\text{O}_y$ (denoted hereafter as $\text{Ag}_x\text{I}_w\text{Bi2201}$ for $n = 1$, $\text{Ag}_x\text{I}_w\text{Bi2212}$ for $n = 2$, and $\text{Ag}_x\text{I}_w\text{Bi2223}$ for $n = 3$, respectively) system to investigate the evolution of superconductivity and ionic conductivity on the variation of Ag and I contents, as well as to understand the structure–property relationship in this regularly interstratified hybrid structure.

In this work, we prepared Ag–I intercalates of high- T_c superconducting $\text{Bi}_2\text{Sr}_2\text{Ca}_{n-1}\text{Cu}_n\text{O}_y$ (denoted hereafter as Bi2201 for $n = 1$, Bi2212 for $n = 2$, and Bi2223 for $n = 3$, respectively) compounds with various Ag and I contents. The relationship between electronic structure and superconductivity was carefully examined by performing systematic X-ray absorption near edge structure (XANES)/extended X-ray absorption fine structure (EXAFS) analyses. On the other hand, the ionic conductivities of these intercalates were also investigated with ac impedance and dc relaxation measurements. To understand their ionic conducting behaviors from the viewpoint of crystal structure, their Ag K -edge EXAFS spectra were analyzed thoroughly on the basis of various structural models. Combining the EXAFS result with one-dimensional electron density calculation, we have

* To whom all correspondence should be addressed. Fax: (82)2-872-9864. Tel: (82)2-880-6658. E-mail: jhchoy@plaza.snu.ac.kr.

suggested not only the intracrystalline structure of the Ag–I intercalant layer but also a reasonable passageway for Ag^+ ionic conduction.

Experimental Section

Sample Preparation. All the pristine compounds $\text{Bi}_2\text{Sr}_2\text{Ca}_{n-1}\text{Cu}_n\text{O}_y$ ($n = 1, 2$, and 3) were prepared through the conventional solid-state reaction,^{7,8} whereas their Ag–I intercalates were synthesized by applying different synthetic methods depending on the phase of host material. In Bi2201 and Bi2212, the intercalation of silver iodide was achieved by heating the mixture pellet of the pristine and Ag metal in an iodine atmosphere ($P_{\text{I}_2} = 1$ atm) as described previously.^{6,9} The heat treatment was carried out in a stepwise manner where the sample was heated in an iodine atmosphere at 170 °C for 3 h and then in air at 190 °C for 10 h. According to the X-ray diffraction (XRD) analysis for the product after the first heat treatment at 170 °C, it was found that no Ag–I intercalate existed but the iodine intercalate, $\text{IBi}_2\text{Sr}_2\text{Ca}_{n-1}\text{Cu}_n\text{O}_y$ (denoted hereafter as IBi2201 for $n = 1$, IBi2212 for $n = 2$, and IBi2223 for $n = 3$, respectively), was formed together with AgI. Such a finding indicates that the Ag–I intercalation is accomplished via the thermal diffusion of Ag^+ ion into the preintercalated iodine sublattice.¹⁰ It is worthy to note here that the reaction between the Ag–I and iodine intercalates could be carried out at an optimum temperature range of 185–200 °C. At the reaction temperature lower than 175 °C, the Ag–I intercalate could be formed with a very slow intercalation kinetics, while at the higher temperature (>210 °C), the final product was obtained as the mixed phase of Ag–I intercalate and iodine intercalate. Therefore we can describe the mechanism in Ag–I intercalation, as follows. When the mixture of Ag–I and iodine intercalates is heated in open air at greater than the boiling point of iodine (184 °C), interlayer iodides are activated and are gradually deintercalated. Then the Ag^+ ion, which is in the α -AgI phase, begins to migrate into the iodine intercalate, during which the interlayer iodide undergoes a spatial rearrangement to form the new Ag–I structure. It is expected that the mobility of intercalated Ag^+ ion is much lower than that in the pure α -AgI, and therefore the Ag^+ intercalation is assumed to be irreversible at ~ 190 °C. At the lower reaction temperature (<175 °C), the iodine intercalate is so stable that it cannot allow the insertion of the Ag^+ ion; on the other hand, at too high a temperature (>210 °C), it seems that the deintercalation of iodine occurs too quickly.

In contrast to the cases of $n = 1$ and 2 , the Ag–I intercalate of Bi2223 could not be synthesized by reacting AgI and IBi2223 at 190 °C in open air, probably because of the slower rate of Ag^+ ion diffusion compared with the deintercalation rate of preintercalated iodine. It originates from the fact that the pristine Bi2223 may not suffer from a large elastic deformation upon Ag^+ intercalation, owing to its thicker unit block with three CuO_2 layers compared with Bi2201 and Bi2212. This difficulty is also ascribed partially to an enhanced attraction between BiO layers induced by the substitution of Bi^{3+} ion with Pb^{2+} .¹¹ To overcome this problem, we adopted an alternative synthetic strategy where a mixture of AgI and IBi2223 was heated at 190 °C for 75 h under an iodine vapor pressure of 1 atm. The single phasic Ag–I–Bi2223 was obtained by both extending the reaction time and imposing an iodine atmosphere to maintain the interlayer iodine content during Ag^+ diffusion. In addition to such chemical methods, it was also possible to intercalate AgI into the Bi-based cuprates with an electrochemical cell of $-\text{IBi}_2\text{Sr}_2\text{Ca}_{n-1}\text{Cu}_n\text{O}_y|\text{Ag}_6\text{I}_4\text{WO}_4|\text{Ag}-$ by applying a constant

current of $10 \mu\text{A}/\text{cm}^2$ at 150 °C. But in this case, the Ag–I intercalate could be obtained in so small an amount (less than ~ 50 mg) from a single batch process that we could perform only the XRD analysis.

Sample Characterization. The formations of single phasic pristine and their Ag–I intercalates were confirmed by XRD analysis using a Phillips PW3710 powder diffractometer equipped with Ni-filtered $\text{Cu-K}\alpha$ radiation ($\lambda_{\alpha 1} = 1.5406$ Å). To determine the amount of guest species introduced into the host lattice, electron microprobe analysis (EPMA) was performed using a JEOL JXA-8600 X-ray analyzer with an $100\text{-}\mu\text{m}$ diameter probe at 20.0 kV and 5.5×10^{-9} A. The evolution of the superconducting property on intercalation was examined by both dc magnetic susceptibility (χ_{dc}) and resistivity measurements. The dc magnetic susceptibilities were measured as a function of temperature with a SQUID magnetometer where the applied field was 10 Oe.¹² Temperature-dependent resistivities were obtained using a conventional four probe method.

Ionic Conductivity Measurement.¹³ Ionic conductivity was measured in the temperature range of 25–270 °C by performing ac impedance and dc relaxation measurements.^{6a} The impedance spectrum was obtained in the entire frequency range of 5 Hz to 13 MHz using the electrochemical cell of $-\text{Ag}|\text{AgI}|\text{Ag}_x\text{I}_y\text{Bi}_2\text{Sr}_2\text{Ca}_{n-1}\text{Cu}_n\text{O}_y|\text{AgI}|\text{Ag}-$, which was connected to a commercial impedance analyzer (HP4192A). The dc relaxation experiment was performed by monitoring the relaxation of cell emf as a function of time with a DMM (Keithley 196A) after switching off a steady-state current supplied by a current source (Keithley 224/2243). A full-impedance plot was then constructed by combining a partial spectrum directly measured and the Fourier-Laplace transform of dc relaxation. The ionic conductivity (σ_i) and the total electrical conductivity (σ_T) could be evaluated from the assignment of the impedance elements on the spectrum.^{6a}

X-ray Absorption Measurement and Data Analyses. X-ray absorption spectroscopic (XAS) analyses were carried out comparatively for $\text{Ag}_{0.76}\text{I}_{1.20}\text{Bi2201}$ (denoted as *L01*), $\text{Ag}_{0.76}\text{I}_{1.17}\text{Bi2212}$ (denoted as *L12*), $\text{Ag}_{1.15}\text{I}_{1.53}\text{Bi2201}$ (denoted as *H01*), $\text{Ag}_{1.17}\text{I}_{1.54}\text{Bi2212}$ (denoted as *H12*), and $\text{Ag}_{1.15}\text{I}_{2.14}\text{Bi2223}$ (denoted as *H23*), to probe the effects of Ag and I contents on the electronic and geometric structures of Ag–I intercalates. The XAS experiments were performed at the beam lines 10B and 7C in Photon Factory (National Laboratory for High Energy Physics, Tsukuba), running at 2.5 GeV with a stored current of 270–360 mA.¹⁴ Samples were finely powdered, mixed with boron nitride (BN) in an appropriate ratio, and pressed into pellets, to obtain an optimum jump ($\mu_i \approx 1$) free from thickness and pinhole effects.¹⁵ All the present spectra were recorded in a transmission mode at room temperature using gas-ionization chambers. The Si (311) channel-cut monochromator was used for the Cu *K*-, Bi *L*₃-, and Ag *K*-edges whereas the Si (111) double-crystal monochromator, detuned by 60% to remove higher harmonics, was used for the I *L*₁-edge.

The data analysis for the present spectra was performed by the standard procedure as follows. The inherent background in the data was removed by fitting a polynomial to the preedge region and extrapolated through the entire spectrum, from which it was subtracted. The resulting spectra, $\mu(E)$, were normalized to an edge jump of unity for comparing the XANES features directly with one another. The absorption spectrum for the isolated atom, $\mu_0(E)$, was approximated by summing the cubic spline. The EXAFS oscillation, $\chi(E)$, was obtained as $\chi(E) = \{\mu(E) - \mu_0(E)\}/\mu_0(E)$. The data were converted to *k* space where the photoelectron wave vector *k* is defined as $k = [2m_e -$

TABLE 1: Chemical Compositions of $\text{Ag}_x\text{I}_w\text{Bi}_2\text{Sr}_2\text{Ca}_{n-1}\text{Cu}_n\text{O}_y$ (Atomic %, EPMA)

$n = 1$							
x^a	Ag (x) ^b	I (w) ^b	Bi	Sr	La	Cu	
1.00	11.07 (0.76)	17.76 (1.20)	29.28	22.05	5.27	14.57	
1.20	12.78 (0.92)	19.01 (1.37)	27.83	21.05	5.19	14.15	
1.30	13.24 (0.97)	18.66 (1.41)	27.27	21.45	5.32	14.02	
1.45	14.30 (1.07)	20.37 (1.52)	26.75	20.61	4.79	13.18	
1.75	15.48 (1.15)	20.07 (1.53)	26.48	20.25	4.65	13.06	
$n = 2$							
x^a	Ag (x)	I (w)	Bi	Sr	Ca	Cu	
1.00	9.56 (0.76)	14.46 (1.17)	22.11	15.14	17.99	20.60	
1.20	11.16 (0.93)	15.59 (1.32)	21.07	13.66	16.75	21.63	
1.30	11.78 (1.00)	15.92 (1.39)	20.76	14.24	17.32	20.25	
1.45	12.85 (1.09)	17.53 (1.52)	20.60	14.08	15.94	18.98	
1.75	13.36 (1.17)	17.33 (1.54)	20.16	13.30	16.04	19.56	
$n = 3$							
x^c	Ag (x)	I (w)	Bi	Pb	Sr	Ca	Cu
1.20	10.01 (1.15)	18.82 (2.14)	14.18	3.80	13.60	15.66	23.79

^a For $n = 1$ and 2, x denotes the initial mixing ratio of Ag to $\text{Bi}_2\text{Sr}_2\text{Ca}_{n-1}\text{Cu}_n\text{O}_y$. ^b For each chemical formula of $\text{Ag}_x\text{I}_w\text{Bi}_2\text{Sr}_2\text{Ca}_{n-1}\text{Cu}_n\text{O}_y$, x and w are given in the parentheses. ^c In $n = 3$, x represents the initial mixing ratio of AgI to IBi2223 .

$(E - E_0)/\hbar^2]^{1/2}$, where m_e is the electron mass, and E_0 is the threshold energy. The resulting $\chi(k)$ oscillation was weighted by a factor of k^r ($r = 2$ for the Ag K -edge and 3 for the Cu K -one) to compensate the attenuation of EXAFS signal with increasing photon energy and Fourier transformed with a Hanning apodization function. To determine structural parameters such as bond distance and coordination number, a nonlinear least-squares curve fitting was carried out to the Fourier first coordination shell EXAFS by using the theoretical formula on the basis of the plane wave single scattering description.¹⁶ The refinements were based on the minimization of F factor, ($F = [\sum k^{2r} \{\chi(k)_{\text{cal.}} - \chi(k)_{\text{exp.}}\}^2]^{1/2}/n$), where $\chi(k)_{\text{exp.}}$, $\chi(k)_{\text{cal.}}$, and n represent the experimental EXAFS oscillation, the fitted oscillation, and the number of data points, respectively.

Results and Discussion

EPMA and Powder XRD. According to the EPMA measurements, it is found that the Ag (x) and I (w) contents exhibit similar dependencies on the initial mixing ratio (x) of $\text{Ag}:\text{Bi}_2\text{Sr}_2\text{Ca}_{n-1}\text{Cu}_n\text{O}_y$ for both $\text{Ag}_x\text{I}_w\text{Bi2201}$ and $\text{Ag}_x\text{I}_w\text{Bi2212}$ compounds (Table 1). In the region of $x \leq 1.45$, the Ag and I concentrations are directly proportional to the x ratio while they remain constant over the range of $x \geq 1.45$. In the Ag–I intercalate of Bi2223 ($H23$), the I content is found to be remarkably higher than those of $\text{Ag}_x\text{I}_w\text{Bi2201}$ ($H01$) and $\text{Ag}_x\text{I}_w\text{Bi2212}$ ($H12$) despite their similar Ag contents. Such a result is surely attributed to the different synthetic conditions of these compounds where $H23$ was prepared under an iodine atmosphere at the stage of final heat treatment whereas $H01$ and $H12$ were synthesized in open air.

Figure 1 shows the powder XRD patterns for the pristines and their Ag–I intercalates.¹⁷ According to the least-squares refinements, the basal increment upon Ag–I intercalation is determined to be ~ 14.6 Å for all of the pristines, which corresponds to the lattice expansion of ~ 7.3 Å per intercalated Ag–I layer. Although the Ag–I intercalation gives rise to a remarkable basal increment which is about twice as large as that of the iodine intercalate ($\Delta d \approx 3.6$ Å),¹⁸ it has little effect on the in-plane a and b lattice parameters.

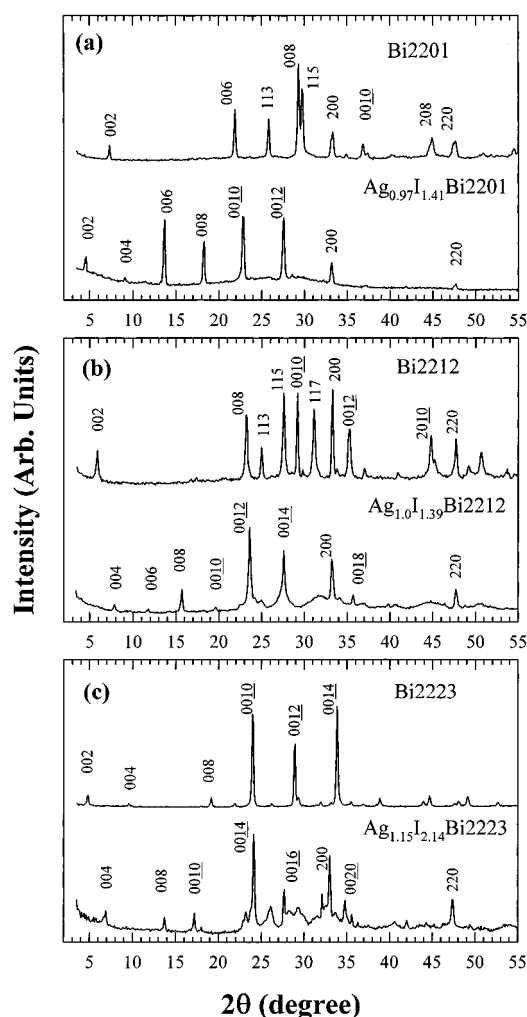


Figure 1. XRD patterns for the pristine $\text{Bi}_2\text{Sr}_2\text{Ca}_{n-1}\text{Cu}_n\text{O}_y$ and their Ag–I intercalates with (a) $n = 1$, (b) $n = 2$, and (c) $n = 3$.

Magnetic Susceptibility. The magnetic susceptibilities of the pristines and their Ag–I intercalates are represented as a function of temperature in Figure 2. Their superconducting transition temperatures (T_c 's) and diamagnetic shielding fractions are summarized in Table 2. All the intercalates are found to exhibit bulk superconductivities with slight T_c depressions of 10–15% compared with those of the pristines. It was previously suggested that the T_c evolution upon intercalation is due to a change in hole concentration of CuO_2 planes¹⁹ and/or due to the weakening of interblock electronic coupling.²⁰ Taking into account the hybrid structure of the Ag–I intercalates, where the electronically insulating Ag–I layer is regularly interstratified between the superconducting host lattices, the interblock electronic coupling is expected to be negligible in these compounds. In this respect, the maintenance of superconductivity upon Ag–I intercalation allows us to conclude that interlayer coupling is not a main factor for superconductivity. Instead, it can be suggested that the present T_c evolution upon intercalation should be rationalized in terms of the charge transfer between guest and host.

Ag K - and I L_1 -Edges XANES. Figure 3 shows the Ag K -edge XANES spectra and their second derivatives of the Ag–I intercalates, together with those of the Ag, AgO, and β -AgI references for comparison. The spectra of the Ag–I intercalates are found to be far from those of Ag and AgO, which rules out the presence of Ag metal and oxygenated Ag^{2+} ion in the intercalated Ag–I sublattice. On the contrary, there

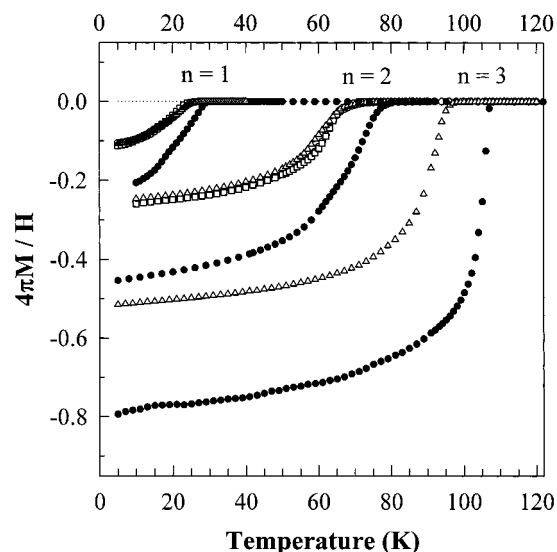


Figure 2. Dc magnetic susceptibilities (χ_{dc} 's) of $\text{Bi}_2\text{Sr}_2\text{Ca}_{n-1}\text{Cu}_n\text{O}_y$ (●) and $\text{Ag}_x\text{I}_{1-x}\text{Bi}_2\text{Sr}_2\text{Ca}_{n-1}\text{Cu}_n\text{O}_y$ (empty symbols). Three compositions have been selected for the intercalates of $n = 1$ with $x = 0.76$ (○), 0.97 (□), 1.15 (△), and $n = 2$ with $x = 0.76$ (○), 1.00 (□), 1.17 (△), respectively.

TABLE 2: In-Plane and Out-of-Plane Lattice Parameters, the Superconducting Transition Temperature (T_c), and the Diamagnetic Shielding Fraction of the Pristine $\text{Bi}_2\text{Sr}_2\text{Ca}_{n-1}\text{Cu}_n\text{O}_y$ and Their Ag–I Intercalates

compound	x	a (Å)	c (Å)	Δc (Å)	T_c (K)	ΔT_c (K)	SVF (%) ^a
$n = 1$							
pristine		5.39	24.23		29		20.6
intercalate	0.76	5.40	38.82	14.59	24.5	4.5	10.6
	0.97	5.40	38.81	14.58	24	5	11.3
	1.15	5.39	38.82	14.59	25	4	10.8
$n = 2$							
pristine		5.40	30.73		80		45.4
intercalate	0.76	5.40	45.40	14.67	67	13	25.3
	1.00	5.40	45.39	14.66	67	13	26.0
	1.17	5.39	45.41	14.68	67	13	24.7
$n = 3$							
pristine		5.40	37.00		107		78.1
intercalate	1.15	5.42	51.60	14.60	95.5	11.5	51.2

^a SVF represents a superconducting volume fraction at 10 K.

are close similarities in the edge energy and spectral feature at multiple scattering regions for the Ag–I intercalates and $\beta\text{-AgI}$, suggesting that the silver is intercalated as a monovalent Ag^+ ion with a $\beta\text{-AgI}$ -like local environment.

The $I L_1$ -edge spectra and their second derivatives for the Ag–I intercalates and some references are represented in Figures 4a and 4b, respectively. All the reference spectra except $\beta\text{-AgI}$ exhibit a characteristic preedge peak A (so-called “white line” type feature) in the 5185–5195 eV region, assigned to the transition from the $2s$ core level to the $5p$ state above the Fermi energy level. Because the intensity of the preedge peak is directly proportional to the density of the unoccupied $I 5p$ final state, it reflects sensitively the oxidation state of the iodine species.^{21,22} In fact, an excellent correlation exists between peak intensity and $5p$ hole density for the references of KIO_4 , KIO_3 , and I_2 , with the formal oxidation states (outermost $5p$ configuration) of I^{7+} ($5p^0$), I^{5+} ($5p^2$), and I^0 ($5p^5$), respectively. In this context, a remarkable depression of the peak A upon iodine intercalation was interpreted as a proof of negatively charged I_3^- species in the IBi2212 lattice.²⁴

However, in contrast to the compounds above, the preedge peak is not observed for $\beta\text{-AgI}$ which is surely due to its completely occupied $I 5p^6$ state. Like $\beta\text{-AgI}$, there is no white

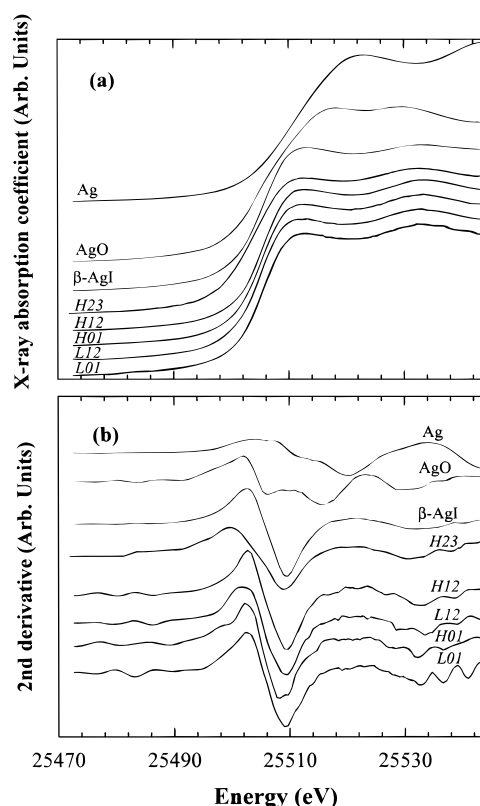


Figure 3. (a) Ag K -edge XANES spectra for Ag–I intercalates of $L01$, $L12$, $H01$, $H12$, and $H23$, and those for some reference compounds, and (b) their second derivative spectra.

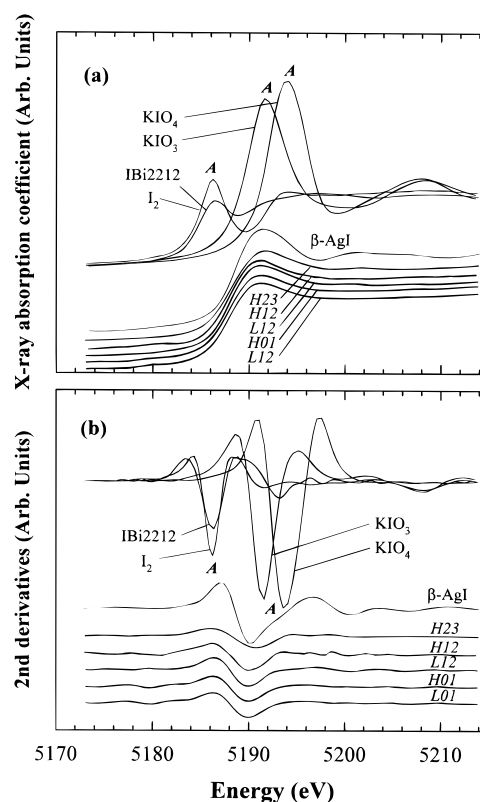


Figure 4. (a) $I L_1$ -edge XANES spectra for Ag–I intercalates of $L01$, $L12$, $H01$, $H12$, $H23$, and those for some reference compounds, and (b) their second derivative spectra.

line feature in the spectra of Ag–I intercalates, clearly indicating that the intercalated iodine species are stabilized as a fully reduced I^- ion. Although the Ag–I intercalates and $\beta\text{-AgI}$ have

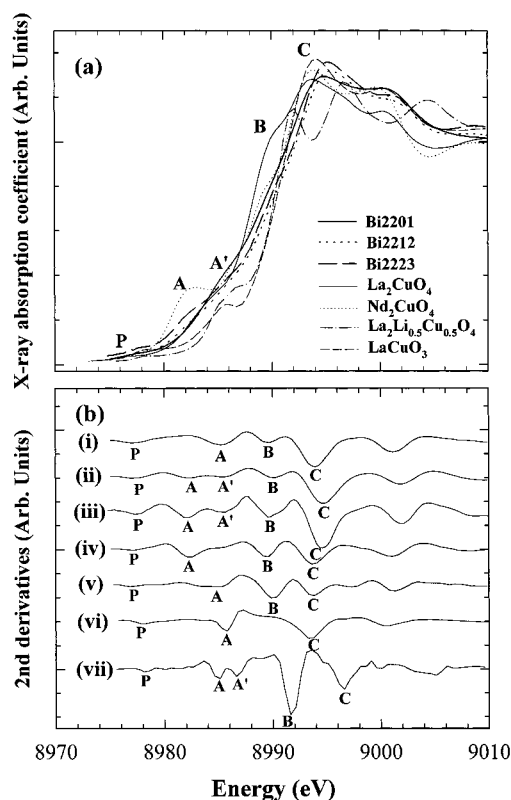


Figure 5. (a) Cu K-edge XANES spectra for the pristines of (i) Bi2201, (ii) Bi2212, and (iii) Bi2223, compared with those for the references of (iv) Nd_2CuO_4 , (v) La_2CuO_4 , (vi) LaCuO_3 , and (v) $\text{La}_2\text{Li}_{0.5}\text{Cu}_{0.5}\text{O}_4$ and (b) their second derivatives.

similar edge positions, they exhibit distinct derivatives in the multiple scattering region above 5196 eV, which points to the different chemical environments around iodine between both compounds.²³

Cu K-Edge XANES and EXAFS. Because the complete assignment of fine features in the Cu K-edge XANES spectra is indispensable for probing the delicate effect of intercalation, we have first attempted to interpret all the spectral fine features of the pristines by comparing them with those of the chemically well-defined copper oxides. Figure 5a represents the Cu K-edge XANES spectra of the pristines, together with those of the references, Nd_2CuO_4 , La_2CuO_4 , LaCuO_3 , and $\text{La}_2\text{Li}_{0.5}\text{Cu}_{0.5}\text{O}_4$, where divalent or trivalent copper ions are stabilized in different local geometries. Although the position of edge jump for Bi2212 and Bi2223 is higher than those of the Cu^{2+} references but lower than those of the Cu^{3+} references, Bi2201 shows nearly the same edge energy as the Cu^{2+} references. Such findings seem to be contradictory to the electronic structure calculation for the $\text{Bi}_2\text{Sr}_{1.6}\text{La}_{0.4}\text{CuO}_y$ compounds ($n = 1, 2$, and 3) where the hole concentration per CuO_2 layer is predicted to decrease rapidly with the increase in number of the CuO_2 plane.²⁴ However, considering the stoichiometry of the present Bi2201 sample, $\text{Bi}_2\text{Sr}_{1.6}\text{La}_{0.4}\text{CuO}_y$, its lower edge energy can be understood as a result of the La^{3+} substitution for Sr^{2+} ion, which significantly decreases the oxidation state of the CuO_2 layer. To differentiate fine spectral features in the Cu K-edge XANES region, the spline spectra were carefully analyzed using the second differential method (Figure 5b).²⁵ All the present compounds show a preedge peak (denoted as P), which is assigned to the quadrupole-allowed transition from the 1s core level to the unoccupied 3d states. The position of the peak P is about 0.3 eV higher for Bi2212 and Bi2223 than that of the Cu^{2+} references but 0.7 eV lower than that of the Cu^{3+}

references, whereas Bi2201 exhibits almost the same peak position as that of the Cu^{2+} references, which is also ascribed to the effect of La^{3+} substitution for Sr^{2+} . In the main edge region, several peaks correspond to the dipole-allowed transitions from the core 1s level to vacant 4p states, which are denoted as A, A', B, and C. According to our previous Cu K-edge XAS study,²⁶ the main-edge features A and B are attributed to the transitions from the 1s orbital to the out-of-plane $4p_\pi$ orbital with and without shakedown processes, respectively, whereas the feature C is ascribed to the transition to the in-plane $4p_\sigma$ orbital without shakedown process. Among them, the shakedown peak A has been known to sensitively reflect the local structure and oxidation state of the CuO_2 layer²⁶ because the ligand-to-metal charge transfer (LMCT) is affected by the number of ligands and the chemical bonding nature of the (M–L) bond. Therefore, the observed order of peak energy among the pristines, $E_A(\text{Bi2201}) > E_A(\text{Bi2212}) > E_A(\text{Bi2223})$, can be understood from the different Cu local symmetries in these compounds; the copper ion in Bi2201 is octahedrally coordinated, whereas those in Bi2212 are stabilized in the CuO_5 square pyramid and those in Bi2223 are partially in the CuO_4 square plane and CuO_5 square pyramid.²⁷ Because an addition of axial oxygen ligand electrostatically reduces the effective LMCT along the c-axis, it gives rise to an upward energy shift of the shakedown peak A. Such an interpretation is supported from the fact that the peak position for Bi2201 is very close to that for the reference La_2CuO_4 with octahedrally coordinated Cu^{2+} ions. However, these peaks are observed at a higher energy side in the trivalent copper compounds (LaCuO_3 and $\text{La}_2\text{Li}_{0.5}\text{Cu}_{0.5}\text{O}_4$) than in the divalent ones, because the Coulombic interaction between nuclei and the core 1s electron is enhanced by higher copper valence. In $\text{La}_2\text{Li}_{0.5}\text{Cu}_{0.5}\text{O}_4$ where the Cu 4p orbitals are split into $4p_\sigma$ and $4p_\pi$ orbitals due to an anisotropic crystal field around copper, the shakedown peak is separated into the peaks A and A', corresponding to the transition of $|1s^2 3d^8\rangle \rightarrow |1s^1 3d^9 4p_\pi^1 L^{-1}\rangle$ and $|1s^2 3d^8\rangle \rightarrow |1s^1 3d^9 4p_\sigma^1 L^{-1}\rangle$, respectively, where L^{-1} denotes a ligand hole. Even though the shakedown process to $4p_\sigma$ orbital hardly occurs in the divalent copper compound, it appears for the trivalent ones through a stronger Coulombic interaction between Cu^{3+} and O^{2-} ions. In this respect, this peak has been regarded as an indicator for the presence of trivalent copper ion.²⁸ As shown in Figure 5b, this peak A' is clearly observed for Bi2212 and Bi2223 but it is not detected for Bi2201, which is in good agreement with the observed order of edge position for the pristines.

On the basis of the assignments above, we have examined the effect of intercalation on the CuO_2 layer by comparing the Cu K-edge XANES spectra of the pristines and their Ag–I intercalates (Figure 6). There clearly is an overall spectral shift of 0.1 eV toward a high-energy side upon Ag–I intercalation into Bi2201, indicating an oxidation of CuO_2 layer. However, no remarkable change in edge position can be detected for the Ag–I intercalates of Bi2212 and Bi2223. Such results are explained by the different number of CuO_2 layer in the unit block (one for Bi2201, two for Bi2212, and three for Bi2223). That is, the amount of hole doping per CuO_2 layer becomes smaller as the number of layers increases. In addition to the overall edge shift, we also observe specific changes in fine features of the Cu K-edge XANES spectra (Figure 6b). Among the main-edge peaks, the peak A shows a remarkable high-energy shift of 0.2–0.3 eV for all the present intercalates, suggestive of a change in the local structure around copper ion, especially, in the bond distance of (Cu–O_{sr}). Because this bond

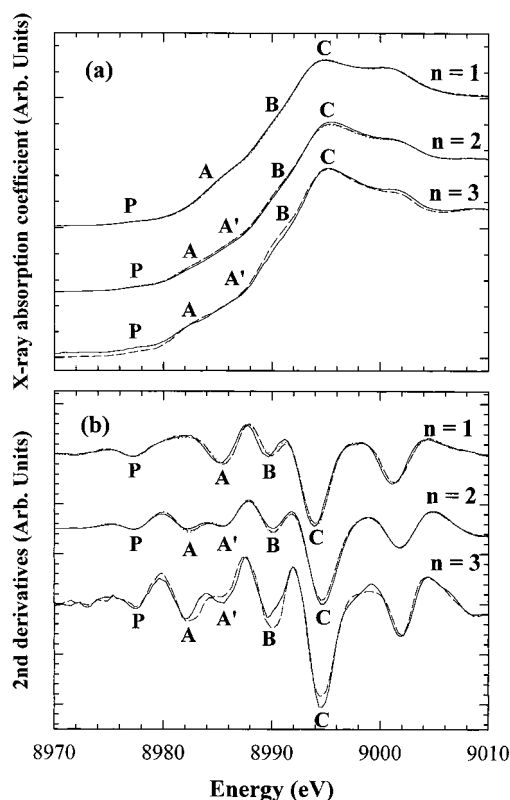


Figure 6. (a) Cu *K*-edge XANES spectra for the pristine $\text{Bi}_2\text{Sr}_2\text{Ca}_{n-1}\text{Cu}_n\text{O}_y$ (—), and their Ag–I intercalates, *L01* (·····), *L12* (·····), *H01* (---), *H12* (- - -), *H23* (- - -), and (b) their second derivatives.

is known to have significant influence on the hole concentration of CuO_2 layer and subsequently on superconductivity,²⁹ we examined quantitatively the effect of intercalation on the local structure of the CuO_2 layer by performing the Cu *K*-edge EXAFS analysis.

The Fourier transforms (FTs) of k^3 -weighted EXAFS spectra for the pristine Bi2201 and Bi2212 and their Ag–I intercalates are represented in Figure 7a.³⁰ The first prominent peak of FT is assigned to the in-plane and out-of-plane (Cu–O) pairs which are overlapped because of their similar bond distances. The first shell due to the (Cu–O) bond was isolated by the inverse Fourier transformation to the *k* space.³¹ The resulting $k^3\chi(k)$ Fourier filtered EXAFS oscillations are shown in Figure 7b, and the curve fittings were carried out to determine the (Cu–O) bond distances.³² The best fits to the first coordination shell are compared with the experimental spectra in Figure 7b, and the calculated structural parameters are listed in Table 3. As shown in the table, the in-plane and out-of-plane (Cu–O) bond distances of Bi2201 are usually decreased upon intercalation. However, in Bi2212, the (Cu–O_{Sr}) bond is shortened whereas the in-plane (Cu–O_p) bond length is almost constant.³³ Such results are consistent with the XANES results where the edge shift upon intercalation is clearly observed for Bi2201 but not for Bi2212. Although it has been well known that the (Cu–O_p) bond distance is closely related to the hole concentration of the CuO_2 layer, its variation was found to be quite minute even with considerable changes in hole concentration of the CuO_2 layer and in *T_c*.³⁴ Compared with the in-plane (Cu–O) bond distance, the out-of-plane (Cu–O) distance sensitively reflects even a small increase in hole concentration of the CuO_2 layer.³⁵ In this regard, the decrease in (Cu–O_{Sr}) bond distance upon Ag–I intercalation can be interpreted as clear evidence of the oxidation of the CuO_2 layer.

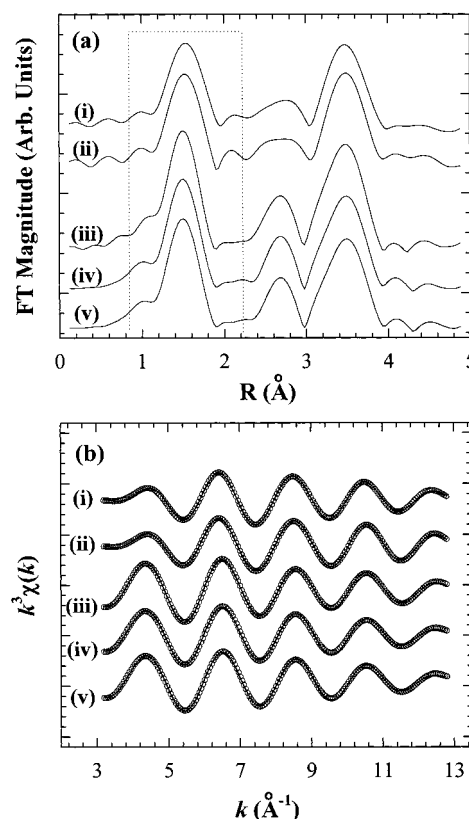


Figure 7. (a) Fourier transforms of the k^3 -weighted Cu *K*-edge EXAFS spectra for (i) the pristine Bi2201, (ii) H01, (iii) the pristine Bi2212, (iv) L12, and (v) H12. Filtering window is indicated by the dashed line. (b) Comparison of the fitted $k^3\chi(k)$ EXAFS spectra at the Cu *K*-edge with the experimental ones. (—: experimental; ○: calculated)

TABLE 3: Results of Nonlinear Least-Square Curve Fitting for the First and Second Shells of Cu *K*-Edge EXAFS Spectra for the Pristine Bi2201 and Bi2212 and Their Ag–I Intercalates

compound	$R_{\text{Cu-O}}$ (Å)		CN ^a		$\sigma^2 (\times 10^{-3} \text{ Å}^2)^b$	
	(Cu–O _p)	(Cu–O _{Sr})	(Cu–O _p)	(Cu–O _{Sr})	(Cu–O _p)	(Cu–O _{Sr})
Bi2201	1.90 ₆	2.39 ₀	4	1	3.1 ₈	17.2 ₇
H01	1.89 ₀	2.37 ₈	4	1	2.8 ₆	15.7 ₀
Bi2212	1.90 ₁	2.36 ₄	4	1	3.2 ₀	4.7 ₀
L12	1.91 ₁	2.34 ₀	4	1	3.8 ₃	9.6 ₈
H12	1.90 ₂	2.34 ₇	4	1	3.5 ₆	5.5 ₄

^a CN represents the coordination number, which is fixed to crystallographic values due to their strong correlation with the Debye–Waller factor. ^b σ^2 represents the Debye–Waller factor.

Bi *L*₃-Edge XANES. Figure 8 shows the Bi *L*₃-edge XANES spectra for the pristine and their intercalates and their second derivatives. The main edge position clearly is shifted by 0.1–0.2 eV toward a high-energy side upon Ag–I intercalation, indicating the oxidation of BiO layer. To obtain detailed information on the local structural variation around bismuth ion induced by intercalation, the spline spectra for the pristine and their intercalates have been carefully examined using the second differential method (Figure 8b). There are three broad peaks, marked as A, B, and C, in all the present spectra, and their energies are summarized in Table 4. Among them, the pre-edge peak A is assigned as the $2p_{3/2} \rightarrow 6s$ transition, and the main-edge peaks B and C in the high-energy region are attributed to the transitions to $6d_{t_2g}$ and $6d_{e_g}$ final states, respectively.^{36,37} As can be seen in the second derivatives, the energy difference between the peaks B and C, $\Delta E (= E_C - E_B)$, is diminished upon intercalation. Even though their energy difference is not

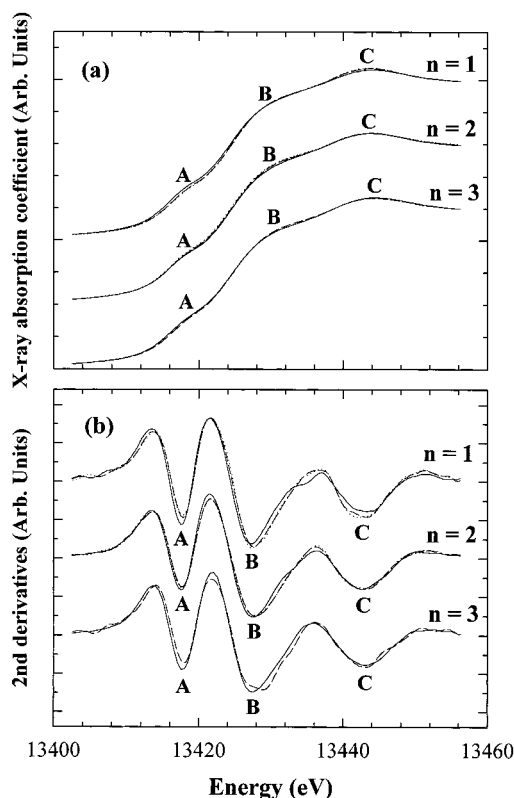


Figure 8. (a) Bi L_3 -edge XANES spectra for the pristines $\text{Bi}_2\text{Sr}_2\text{Ca}_{n-1}\text{Cu}_n\text{O}_y$ (—), and their Ag–I intercalates, L01 (····), L12 (— · — ·), H01 (---), H12 (---), and H23 (---), and (b) their second derivatives.

TABLE 4: Peak Energies of the Bi L_3 -Edge XANES Spectral Features (A, B, and C) for the Pristines and Their Ag–I Intercalates

compound	E_A (eV) ^a	E_B (eV) ^a	E_C (eV) ^a	$E_C - E_B$ (eV)
Bi2201	13417.5	13428.4	13443.0	14.6
L01	13417.7	13428.9	13442.8	13.9
H01	13417.7	13428.9	13442.8	13.9
Bi2212	13417.5	13428.1	13442.8	14.7
L12	13417.6	13428.5	13442.8	14.3
H12	13417.6	13428.5	13442.8	14.3
Bi2223	13417.8	13427.4	13442.9	15.5
L23	13418.0	13428.2	13443.0	14.8

^a Peak energies are determined from the peak positions of the second derivative spectra.

exactly equal to the ground-state crystal field parameter ($10Dq$), the peak splitting is surely proportional to the crystal field strength.^{38,39} Therefore, the observed decrease in ΔE indicates the weakening of the crystal field around Bi upon intercalation which may originate from the following two effects. One is the effect of introducing the guest layer inbetween the Bi_2O_2 double layer, in which axially coordinated oxygen in the adjacent BiO layer is replaced by the intercalated iodine. Because the electronegativity of iodine is smaller than that of oxygen, the crystal field strength around the bismuth ion is decreased upon intercalation. The other effect is that of increasing the ($\text{Bi}-\text{O}_{\text{S}}$) bond distance, which is expected from the Cu K -edge EXAFS results. Because the apical oxygen is coordinated simultaneously to copper ion in one direction and to bismuth ion on the opposite side,²⁷ a remarkable shortening of the ($\text{Cu}-\text{O}_{\text{S}}$) bond distance results in an increase of the competing ($\text{Bi}-\text{O}_{\text{S}}$) bond distance and thus a weakening of the crystal field around Bi. In fact, such a decrease in ΔE has been observed generally for all the known intercalation compounds of Bi-based cuprates such as halogen, mercuric salt, and new organic salt

intercalates.⁵ In this respect, it is claimed that this phenomenon should be approved as a proof for the intercalation of guest species into the interlayer space of the Bi_2O_2 layer.

From the present XANES/EXAFS results, it is clear that there is a charge transfer between host and guest, giving rise to a partial oxidation of the CuO_2 and BiO layers. Because the present I L_1 - and Ag K -edge XANES analyses indicate that the intercalated Ag and I species are stabilized as Ag^+ and I^- ions, respectively,⁴⁰ the difference ($w-x$) in $\text{Ag}_x\text{I}_w\text{Bi}_2\text{Sr}_2\text{Ca}_{n-1}\text{Cu}_n\text{O}_y$ is considered as a degree of net hole donation to the host block. According to the EPMA results, the ($w-x$) value is determined to be 0.38–0.44 for $\text{Ag}_x\text{I}_w\text{Bi}_2201$, 0.37–0.41 for $\text{Ag}_x\text{I}_w\text{Bi}_2212$, and 0.99 for $\text{Ag}_x\text{I}_w\text{Bi}_2223$. In contrast to $\text{Ag}_x\text{I}_w\text{Bi}_2201$ and $\text{Ag}_x\text{I}_w\text{Bi}_2212$ systems, this value is significantly larger for the $\text{Ag}_x\text{I}_w\text{Bi}_2223$ system than for the iodine intercalate of $0.33e^-$ which was evaluated by both Hall coefficient measurement^{21b} and Raman spectroscopic studies.⁴¹ Therefore, it is reasonably predicted that the T_c depressions for $\text{Ag}_x\text{I}_w\text{Bi}_2201$ and $\text{Ag}_x\text{I}_w\text{Bi}_2212$ would be similar to or slightly larger than those for the corresponding iodine intercalates whereas, in Bi_2223 , the T_c decrease upon Ag–I intercalation would be more pronounced than that upon iodine intercalation. Such a prediction is clearly confirmed by comparing the present T_c depressions for the Ag–I intercalates with the previously reported T_c depressions for the iodine intercalates.^{18–20,42} It is therefore concluded that T_c variations in $\text{Ag}_x\text{I}_w\text{Bi}_2\text{Sr}_2\text{Ca}_{n-1}\text{Cu}_n\text{O}_y$ and $\text{IBi}_2\text{Sr}_2\text{Ca}_{n-1}\text{Cu}_n\text{O}_y$ are well correlated with the degrees of hole doping.

Ionic Conductivity. The ionic conductivities (σ_i 's) of $\text{Ag}_x\text{I}_w\text{Bi}_2\text{Sr}_2\text{Ca}_{n-1}\text{Cu}_n\text{O}_y$ with $n = 1, 2$, and 3 are plotted in Figure 9a–c as functions of temperature, together with that of the reference AgI. As reported previously,⁴³ a sharp phase transition of $\alpha \leftrightarrow \beta$ is observed at 147 °C for AgI, which confirms reliability of the present measurement. In the Ag–I intercalates, there is a significant enhancement of σ_i with an increase in Ag content (x) for the entire temperature range, but they exhibit similar temperature dependencies of σ_i , with the activation energy (ΔE_a) of 0.22 ± 0.02 eV. From these similar and relatively low ΔE_a values for the Ag^+ conduction in $\text{Ag}_x\text{I}_w\text{Bi}_2\text{Sr}_2\text{Ca}_{n-1}\text{Cu}_n\text{O}_y$, we can assume that all the intercalates possess either a high concentration of defects or an energetically favored anion network, depending on the guest Ag and I concentrations. Although all the intercalates are synthesized under the same synthetic condition, they can have a different type of lattice defects in the interlayer Ag–I lattice. As summarized in Table 1, the stoichiometry ratio of Ag to I (x/w) gradually decreases with the decrease of x , which implies that there is a substantial amount of cation vacancies in the intercalates with lower Ag and I concentrations. On the other hand, in the intercalate with the highest guest concentration, Ag and I are almost saturated within the interlayer space, where we can expect the distortion of the anion lattice and/or the increase of interstitial cations. Therefore, it can be qualitatively understood that all the Ag–I intercalates contain the lattice defects in a significant level, resulting in the similar ΔE_a values of ionic conductivity.

Because the ionic conductivity is governed not only by ΔE_a but also by the carrier concentration (n),⁴⁴ the increase in σ_i with increasing x should be attributed mainly to a change in n corresponding to the Ag^+ concentration in the interstitial site. It is well known that the fraction of interstitial Ag^+ cation (n) is determined statistically from the relation, $n = x \cdot \exp(-\Delta E_p/RT)$,⁴⁵ where x and ΔE_p represent the total Ag^+ concentration in the normal and interstitial lattice sites and the potential barrier between both sites, respectively. The observed correlation

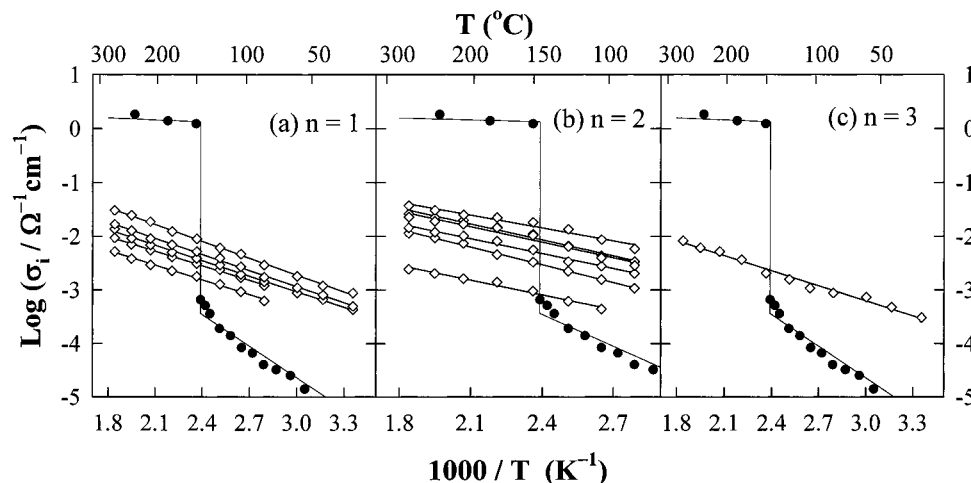


Figure 9. The temperature-dependent ionic conductivities of $\text{Ag}_x\text{I}_n\text{Bi}_2\text{Sr}_2\text{Ca}_{n-1}\text{Cu}_n\text{O}_y$, with (a) $n = 1$, $x = 0.76, 0.92, 0.97, 1.07$, and 1.15 ; (b) $n = 2$, $x = 0.76, 0.93, 1.00, 1.09$, and 1.17 ; and (c) $n = 3$, $x = 1.15$, are represented, together with the experimental (●) and literature data⁴⁴ (—) for AgI.

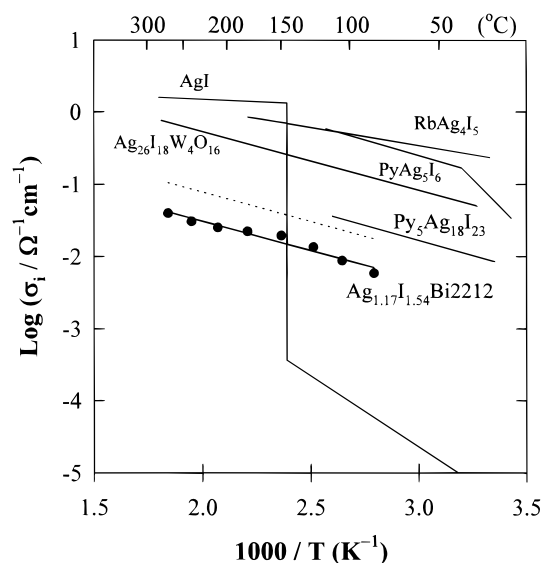


Figure 10. Comparison of the ionic conductivity of *H12* with those of some superionic conductors.^{47–49} Dotted line represents the σ_i of *H12* multiplied by 2.5 for comparison with that of $\text{Py}_5\text{Ag}_{18}\text{I}_{23}$.

between σ_i and x in the Ag–I intercalates can be an indication of the similarity of the conduction pathway for all the solid solution range, giving rise to nearly the same ΔE_p .

To evaluate the ionic conductivity of the intercalates, the temperature-dependent σ_i for *H12* is compared with those for several Ag⁺ superionic conductors, AgI, RbAg_4I_5 , KAg_4I_5 , PyAg_5I_6 (Py = pyridinium), $\text{Py}_5\text{Ag}_{18}\text{I}_{23}$, and $\text{Ag}_{26}\text{I}_{18}\text{W}_4\text{O}_{16}$ (Figure 10).^{46,47} The figure clearly shows that the *H12* compound has an excellent ionic conductivity which is similar to those of other superionic conductors. Among the present superionic conductors, $\text{Py}_5\text{Ag}_{18}\text{I}_{23}$ is a two-dimensional solid electrolyte due to its anisotropic crystal structure where the pyridinium ion blocks the diffusion of Ag⁺ ions along the *c*-axis just as the host lattice in Ag–I intercalate. Such a two-dimensional ionic conductor has a conduction mechanism quite different from that of the three-dimensional one, because the former has fewer sites available for mobile carrier and a more reduced dimensionality in conduction space than the latter. For this reason, it is reasonable to compare the ionic conductivity of *H12* with that of the two-dimensional Ag⁺-conductor, $\text{Py}_5\text{Ag}_{18}\text{I}_{23}$. As shown in Figure 10, the σ_i of $\text{Py}_5\text{Ag}_{18}\text{I}_{23}$ is slightly higher than that of *H12*, which is attributable to their different

TABLE 5: Ionic Conducting Properties of Ag⁺ Ionic Conductors

Ag ⁺ conductor	σ_i ($\Omega^{-1}\text{cm}^{-1}$) ^a	ΔE_a (eV)	t_i ^b	ref
<i>H23</i>	$10^{-2.0}$	0.20 ₇	0.60	this work
<i>H12</i>	$10^{-1.4}$	0.21 ₄	0.40	this work
<i>H01</i>	$10^{-1.5}$	0.21 ₅	0.28	this work
<i>L12</i>	$10^{-2.6}$	0.22 ₈	0.02	this work
<i>L01</i>	$10^{-2.3}$	0.20 ₉	0.12	this work
α -AgI	$10^{0.21}$ (200 °C)	0.10	>0.9999	this work, 43
RbAg_4I_5	$10^{-0.52}$ (30 °C)	0.09	>0.9999	46
$(\text{C}_5\text{H}_5\text{NH})_5\text{Ag}_{18}\text{I}_{23}$	$10^{-1.44}$ (120 °C)	0.21	>0.9999	47c
α - Ag_2HgI_4	$10^{-2.70}$ (60 °C)	0.33	>0.9999	48
$\text{Ag}^+/\beta\text{-Al}_2\text{O}_3$	$10^{-1.25}$ (270 °C)	0.19	>0.9999	49

^a The σ_i and t_i data for the Ag–I intercalates are taken at 270 °C.

^b Ionic transference number ($t_i = \sigma_i/\sigma_T$) represents the partial ionic contribution to the total electric conductivity.

Ag⁺ concentrations where the Ag⁺ content of $\text{Py}_5\text{Ag}_{18}\text{I}_{23}$ ($8.9 \times 10^{21}\text{ cm}^{-3}$) is about 2.5 times higher than that of *H12* ($3.5 \times 10^{21}\text{ cm}^{-3}$). In fact, the hypothetical σ_i (dotted line) of *H12*, which is multiplied by 2.5, shows a close proximity and a similar slope to the σ_i of $\text{Py}_5\text{Ag}_{18}\text{I}_{23}$. It implies that the present intercalate, *H12* has an ionic conducting property similar to those of the previous AgI-based superionic conductors, where the nature of iodide network plays an important role in ion transport.⁵⁰

The σ_i , ΔE_a , and ionic transference number ($t_i = \sigma_i/(\sigma_i + \sigma_e)$) of the Ag–I intercalates are summarized in Table 5, in comparison with those of the well-known superionic conductors. In contrast to the high t_i of superionic conductors (≈ 1), the Ag–I intercalates exhibit the t_i values of 0.02–0.60 at 270 °C, indicating an excellent mixed conductivity, which is surely due to their unique hybrid structure consisting of an ionic conducting Ag–I layer and an electronic conducting host layer as illustrated in Figure 11. On the basis of such findings, these intercalates are expected to be useful as electrode materials in various electrochemical devices. Moreover, the t_i of the Ag–I intercalate is also found to depend strongly on the chemical composition, which enables us to control freely the proportion of σ_i to σ_e by adjusting the mixing ratio (x) of Ag and the pristine.

Ag K-Edge EXAFS. Figure 12a represents the FTs of k^2 -weighted EXAFS spectra for $\text{Ag}_x\text{I}_n\text{Bi}_2\text{Sr}_2\text{Ca}_{n-1}\text{Cu}_n\text{O}_y$ ($n = 1, 2$, and 3) and the reference β -AgI. For all the present compounds, a doubly split feature is commonly observed at around 2.0 and 2.6 Å,⁵¹ which is attributed to the silver–iodine

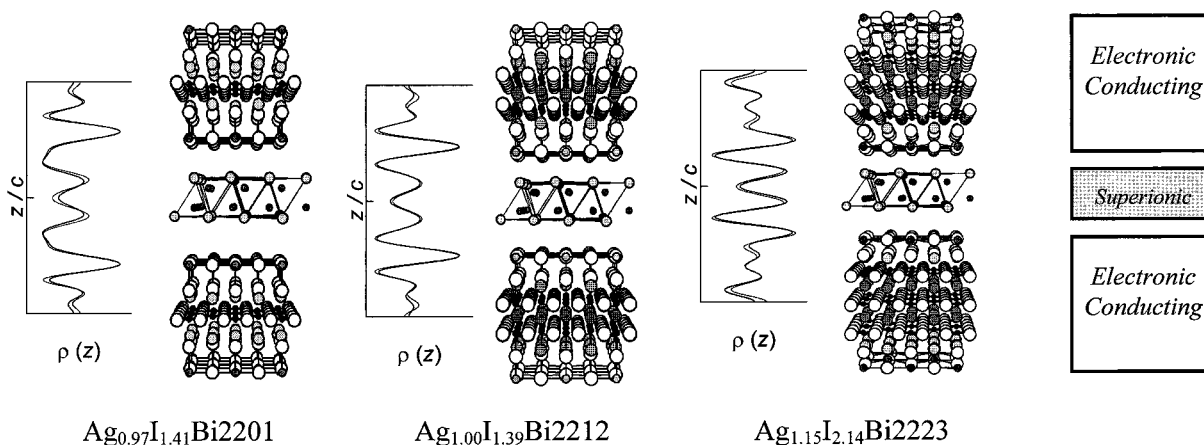


Figure 11. Crystal structures of $\text{Ag}_{0.97}\text{I}_{1.41}\text{Bi2201}$, $\text{Ag}_{1.00}\text{I}_{1.39}\text{Bi2212}$, and $\text{Ag}_{1.15}\text{I}_{2.14}\text{Bi2223}$, and their theoretical one-dimensional Fourier electron density maps calculated from the present structural model (represented as thick solid lines) and the experimental ones from the observed XRD (00l) intensities (thin solid lines). For all three compounds, the resolution of experimental data is ~ 1.75 Å, and the reliability factor, $R (= [\sum_c(\rho_{\text{cal.}} - \rho_{\text{obs.}})^2]^{1/2} / \sum_c \rho_{\text{obs.}})$, is determined to be less than 5%.

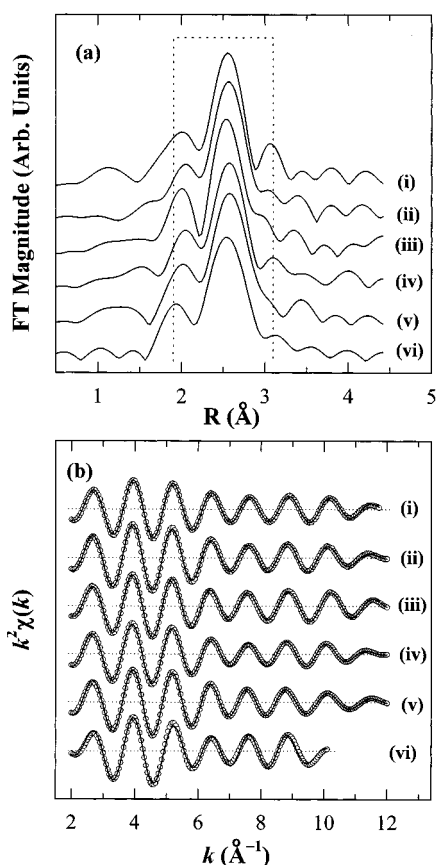


Figure 12. (a) Fourier transforms of the k^2 -weighted Ag K -edge EXAFS spectra for (i) $H23$, (ii) $H12$, (iii) $H01$, (iv) $L12$, (v) $L01$, and (vi) $\beta\text{-AgI}$. Filtering window is indicated by the dashed lines. (b) Comparison between experimental and fitted $k^2\chi(k)$ EXAFS spectra, (—, experimental; O, calculated).

bonding pair. This first coordination shell was isolated by inverse Fourier transformation to the k space. The resulting Fourier filtered $k^2\chi(k)$ EXAFS oscillations are shown in Figure 12b, and curve fitting was carried out to determine structural parameters such as coordination number (CN), bond distance ($R_{\text{Ag-I}}$), and Debye–Waller factor (σ^2). As shown in Figure 12b, the amplitude and oscillation frequency of Ag–I intercalates are nearly the same as those of $\beta\text{-AgI}$, implying that the intercalated silver ion has a local environment similar to that of $\beta\text{-AgI}$. The best fitting results to the first coordination shell

TABLE 6: Structural Parameters Calculated from the Nonlinear Curve Fitting to the Ag K -Edge EXAFS Spectra

compound	$\Delta R_{\text{filtered}}$ (Å) ^a	CN ^b	$R_{\text{Ag-I}}$ (Å)	$\sigma^2 (\times 10^{-3} \text{ Å}^2)^c$
$H23$	1.902–3.068	2.70	2.75 ₀	7.3
		1.09	2.90 ₁	8.5
$H12$	1.902–3.099	3.17	2.76 ₂	13.2
		0.95	2.91 ₁	6.2
$H01$	1.871–3.068	2.88	2.76 ₉	5.4
		1.02	2.94 ₃	2.0
$L12$	1.902–3.129	4.14	2.78 ₃	13.2
$L01$	1.902–3.037	4.22	2.78 ₇	10.4
$\beta\text{-AgI}$	1.871–3.283	4 ^d	2.78 ₀	11.3

^a $\Delta R_{\text{filtered}}$ represents the range of inverse Fourier transform. ^b CN represents the coordination number. ^c σ^2 represents the Debye–Waller factor. ^d The CN for $\beta\text{-AgI}$ is fixed to the crystallographic value to obtain the amplitude reduction factor, which is used for determining CN of Ag in the Ag–I intercalates.

are compared with the experimental spectra in Figure 12b, and the obtained structural parameters are summarized in Table 6. Although the fitting analyses based on the crystal structure of $\beta\text{-AgI}$ allow us to reproduce the experimental data of $L01$ and $L12$ very well, those analyses give relatively poor fits for $H01$, $H12$, and $H23$. Therefore, we have attempted alternatively to fit the experimental spectra by using different structural models with a displacement of the Ag^+ ion from the center of the iodine tetrahedron or the deformation of iodine tetrahedron. Among them, the model with a displacement of Ag toward a face of the iodine tetrahedron is found to give the best fits to $H01$, $H12$, and $H23$. In fact, such a distorted structure has been also observed for $\alpha\text{-AgI}$, which originates from the highly mobile nature of Ag^+ ion in the quasimolten iodide lattice. However, the origin of structural deformation in the present Ag–I intercalates ($H01$, $H12$, and $H23$) is suggested to be the enhanced strain between Ag^+ ions induced by the increase in Ag content.

As listed in Table 6, there are few differences among the (Ag–I) bond distances of $L01$ (2.78₇ Å) and $L12$ (2.78₃ Å) and that of $\beta\text{-AgI}$ (2.78₀ Å).⁵² On the other hand, the (Ag–I) bond lengths of $H01$, $H12$, and $H23$ are determined to be 2.75₀–2.76₉ Å for three iodines and 2.90₁–2.94₃ Å for the other one, which are very similar to the previously reported values of $\alpha\text{-AgI}$ (2.78₁ Å \times 3 and 2.93₁ Å \times 1).⁵³ Such results confirm that the local structure of the intercalated Ag–I layer is changed from the regular tetrahedron to a distorted one, like in $\alpha\text{-AgI}$, as the Ag content increases.

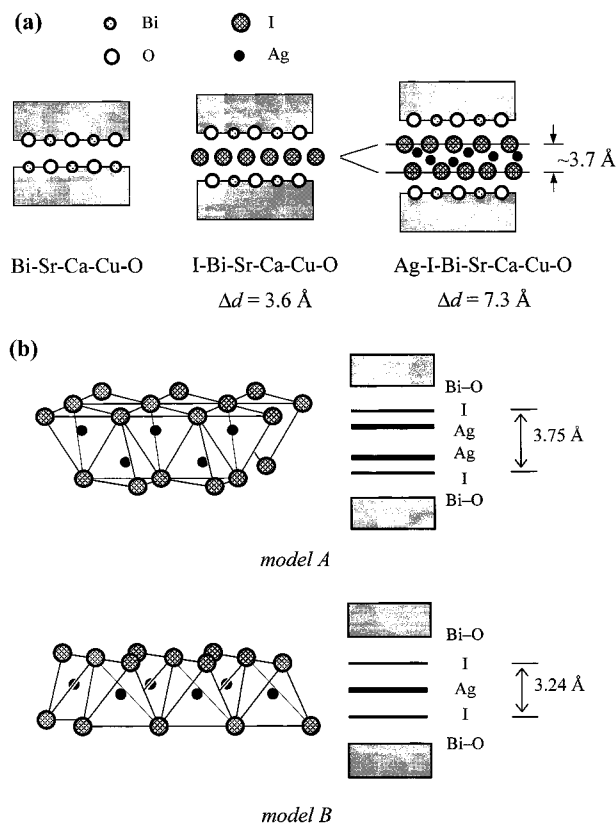


Figure 13. (a) Schematic representation of structural evolution upon intercalation of iodine and Ag-I into the Bi-Sr-Ca-Cu-O lattice. (b) Intracrystalline structure models for AgI_4 tetrahedra sharing edges (model A) or corners (model B). In the latter, the silver ions form a monolayer inbetween the iodine layers, while they form double layers in the former.

One-Dimensional Fourier Map and Structure Modeling.

On the basis of present EXAFS results, the structural model of the Ag-I sublattice has been proposed by considering an available interlayer space and a volume demand for the two-dimensional array of AgI_4 tetrahedra. Because the basal spacing of the Ag-I intercalate indicates the presence of an iodine double layer in the interlayer space, the Ag-I sublattice should consist of the monolayer of AgI_4 tetrahedra. Figure 13 demonstrates the most probable orientations for AgI_4 tetrahedra, together with the schematic diagram of structural evolution upon intercalation. From the (Ag-I) bond distance obtained by EXAFS analysis, the projected I-I distance along the *c*-axis is estimated to be 3.75 Å and 3.24 Å for the models A and B, respectively. As shown in Figure 13a, the height of the Ag-I layer in model A is consistent with the gallery height (~3.7 Å) calculated by subtracting the basal spacing of iodine intercalate (~3.6 Å) from that of Ag-I intercalate (~7.3 Å), suggestive of the suitability of model A. To confirm the reliability of this structure, one-dimensional electron density maps obtained in two different ways are compared⁵⁴: one is calculated using the structure factor (F_{00l}) obtained from the (*00l*) reflection intensities in the XRD patterns of $\text{Ag}_x\text{I}_y\text{Bi}_2\text{Sr}_2\text{Ca}_{n-1}\text{Cu}_n\text{O}_y$ ⁵⁵, and the other is simulated on the basis of the present model. As shown in Figure 11, there is excellent accordance between the experimental electron density profiles and the calculated ones, which clarifies the reliability of the model A.

On the basis of the model A, the expanded structure of the intercalated Ag-I layer is illustrated in Figure 14, where an AgI_4 tetrahedron shares its faces with three neighboring octahedra and its edges with four tetrahedra. Although the

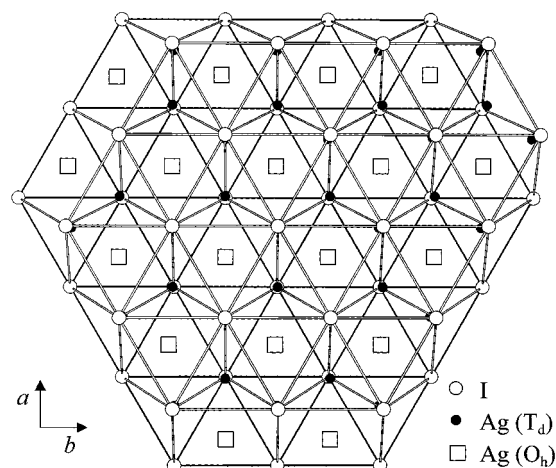


Figure 14. Illustration of the tetrahedral (●) and octahedral sites (□) for the migration of Ag^+ ion within the interlayer Ag-I sublattice.

complete occupation of the tetrahedral site (T_d) by Ag^+ ion results in the Ag/I ratio of unity, EPMA reveals that this ratio has the value of 0.54–0.76 for all the Ag-I intercalates, indicating that the intercalated Ag^+ ion cannot occupy all T_d 's due to a considerable $\text{Ag}^+ - \text{Ag}^+$ repulsion. In fact, it has been found from the Ag *K*-edge EXAFS analyses that the Ag^+ ion in the Ag-I intercalates with high Ag contents (*H01* and *H12*) is displaced from the center of T_d toward a face shared by octahedra, which is interpreted as a result of Coulombic interaction among Ag^+ ions. Because such a repulsive interaction forces the Ag^+ ion to move toward the crystal site with lower potential energy, the direction of Ag^+ displacement in the Ag-concentrated compound implicates the most favorable conduction pathway. In this respect, it is suggested that the Ag^+ ion in the intercalated Ag-I sublattice migrates along the line of $\cdots T_d - O_h - T_d - O_h - T_d \cdots$, even though the occupancy of the octahedral site (O_h) is relatively low compared with T_d . In fact, such a conduction pathway including O_h has already been proposed for most of the ionic conducting AgI-related compounds.^{46,47,56} To confirm the reliability of this conduction model, in situ Ag *K*-edge EXAFS analysis at elevated temperatures are underway.

Conclusion

We have developed new mixed conducting nanohybrids, $\text{Ag}_x\text{I}_y\text{Bi}_2\text{Sr}_2\text{Ca}_{n-1}\text{Cu}_n\text{O}_y$ ($0.76 \leq x \leq 1.17$; $n = 1, 2$, and 3), by intercalating the superionic conducting Ag-I layer into the superconducting $\text{Bi}_2\text{Sr}_2\text{Ca}_{n-1}\text{Cu}_n\text{O}_y$ lattice. According to systematic XANES/EXAFS analyses, it is found that the CuO_2 and BiO layers are slightly oxidized upon intercalation because of the charge transfer between host and guest. An excellent correlation between the T_c depression and the amount of hole doping is also revealed for the Ag-I and iodine intercalates. Based on such findings, it is concluded that the T_c evolution upon intercalation originates mainly from an increase in hole concentration. On the other hand, ac impedance and dc relaxation analyses show that all the Ag-I intercalates have high σ_e and σ_i , which strongly depend on guest concentration and temperature. Because the proportion of σ_i to σ_e can be freely controlled by adjusting the mixing ratio of Ag and the pristine, the Ag-I intercalate is expected to be very useful as an electrode material in various electrochemical devices. In addition, from the viewpoint of crystal structure, the excellent mobility of Ag^+ ion is well understood from the Ag *K*-edge EXAFS results, indicating that the intercalated Ag^+ ion is

stabilized in a tetrahedral site, as in superionic conducting AgI. Combining the present EXAFS analyses with one-dimensional electron density mapping, we suggest the conducting pathway for Ag^+ ion as well as the intracrystalline structure of the Ag–I intercalant layer. From the present study, it is manifest that the intercalation technique provides an effective method to develop various kinds of nanohybrids with useful physical properties.

Acknowledgment. This work was supported in part by the Korean Ministry of Education (BSRI-97-3413) and by the Korea Science and Engineering Foundation through the Center for Molecular Catalysis. We thank Prof. S. I. Lee and M. K. Bae (POSTECH) for the T_c measurements.

References and Notes

- (1) Weber, W. J.; Tuller, H. L.; Mason, T. O.; Cormack, A. N. *Mater. Sci. Eng. B* **1993**, *18*, 52–71.
- (2) Heyne, L. In *Solid Electrolytes*; Geller, S., Ed.; Springer-Verlag: New York, 1977; pp 185–189.
- (3) Rao, C. N. R. *Mater. Sci. Eng. B* **1993**, *18*, 1–21.
- (4) (a) Choy, J.-H.; Park, N.-G.; Hwang, S.-J.; Kim, D.-H.; Hur, N.-H. *J. Am. Chem. Soc.* **1994**, *116*, 11564–11565. (b) Choy, J.-H.; Park, N.-G.; Hwang, S.-J.; Khim, Z.-G. *J. Phys. Chem.* **1996**, *100*, 3783–3787.
- (5) (a) Choy, J.-H.; Hwang, S.-J.; Park, N.-G. *J. Am. Chem. Soc.* **1997**, *119*, 1624–1633. (b) Bae, M.-K.; Kim, M.-S.; Lee, S.-I.; Choy, J.-H.; Park, N.-G.; Hwang, S.-J.; Kim, D.-H. *Phys. Rev. B* **1996**, *53*, 12416–12421. (c) Choy, J.-H.; Hwang, S.-J.; Kim, D.-K. *Phys. Rev. B* **1997**, *55*, 5674–5677.
- (6) (a) Choy, J.-H.; Park, N.-G.; Kim, Y.-I.; Hwang, S.-H.; Lee, J.-S.; Yoo, H.-I. *J. Phys. Chem.* **1995**, *99*, 7845–7848. (b) Choy, J.-H.; Park, N.-G.; Kim, Y.-I.; Kim, C.-H. *Eur. J. Solid State Inorg. Chem.* **1995**, *132*, 701–708. (c) Choy, J.-H.; Park, N.-G.; Hwang, S.-J.; Kim, Y.-I. *Synth. Met.* **1995**, *71*, 1551–1553.
- (7) Maeda, A.; Hase, M.; Tsukada, I.; Noda, K.; Takebayashi, S.; Uchinokura, K. *Phys. Rev. B* **1990**, *41*, 6418–6434.
- (8) The nominal compositions for the pristine with $n = 1, 2$, and 3 are $\text{Bi}_2\text{Sr}_{1.6}\text{La}_{0.4}\text{CuO}_y$, $\text{Bi}_2\text{Sr}_{1.5}\text{Ca}_{1.5}\text{Cu}_2\text{O}_y$, and $\text{Bi}_{1.85}\text{Pb}_{0.35}\text{Sr}_{1.9}\text{Ca}_{2.1}\text{Cu}_3\text{O}_y$, respectively. In each formula, the oxygen content (y) is estimated as $2n + 4 + \delta$ ($0 < \delta < 0.4$).
- (9) The silver metal and pristine were mixed in various ratios of 1.00, 1.20, 1.30, 1.45, and 1.75, and then heated at 840 °C for 3 h to obtain better surface contact between the reactant grains.
- (10) This argument was further supported by the fact that the single phasic Ag–I intercalates can be synthesized by reacting the iodine intercalates with AgI at 190 °C.
- (11) (a) Gopinath, C. S.; Subramanian, S. *Physica C* **1991**, *176*, 331–335. (b) Liu, R.; Klein, M. V.; Han, P. D.; Payne, D. A. *Phys. Rev. B* **1992**, *45*, 7392–7396. (c) Calestani, G.; Francesconi, M. G.; Salsi, G.; Andreotti, G. D.; Migliori, A. *Physica C* **1993**, *197*, 283–298.
- (12) To verify the dependence of T_c upon Ag and I contents, the magnetic susceptibilities of Ag–I intercalates were measured for $\text{Ag}_x\text{I}_y\text{Bi}_2\text{Bi}_2\text{O}_{11}$ with $x = 0.76, 0.97$, and 1.15 , and $\text{Ag}_x\text{I}_y\text{Bi}_2\text{Bi}_2\text{O}_{11}$ with $x = 0.76, 1.00$, and 1.17 , respectively.
- (13) The ionic conducting behavior of intercalated Ag–I species was also checked by performing the conductivity measurements by the pulsed dc polarization methods with the cell of $-\text{Pt}[\text{Au}(\text{Ag}_x\text{I}_y\text{Bi}_2\text{Sr}_2\text{Ca}_{n-1}\text{Cu}_n\text{O}_y)]-\text{Au}|\text{Pt}-$. In this ion-blocking cell configuration, the electronic conductivity (σ_e) could be measured under the dc due to the polarization effect, whereas under the pulsed current (10 μs width, 10 Hz), total electrical conductivity (σ_T) could be monitored from the contribution of all the mobile species. The ionic conductivity was then calculated as $\sigma_i = \sigma_T - \sigma_e$.
- (14) (a) Oyanagi, H.; Matsushida, T.; Ito, M.; Kuroda, H. *KEK Report* **1984**, *83*, 30. (b) Kuroda, H.; Koyama, A. *KEK Report* **1989**, *84*, 19.
- (15) Stern, E. A.; Kim, K. *Phys. Rev. B* **1981**, *23*, 3781.
- (16) Teo, B. K. *EXAFS: Basic Principles and Data Analysis*; Springer-Verlag: Berlin, 1986; pp 114–141.
- (17) In the Ag–I intercalates of $\text{Bi}_2\text{Bi}_2\text{O}_{11}$ and $\text{Bi}_2\text{Bi}_2\text{O}_{11}$, the XRD patterns are demonstrated only for $\text{Ag}_{0.97}\text{I}_{1.41}\text{Bi}_2\text{Bi}_2\text{O}_{11}$ and $\text{Ag}_{1.00}\text{I}_{1.39}\text{Bi}_2\text{Bi}_2\text{O}_{11}$, because the other compositions show nearly the same pattern except for minute variations in relative (001) intensities.
- (18) (a) Xiang, X.-D.; McKernan, S.; Vareka, W. A.; Zettl, A.; Corkill, J. L.; Barbee III, T. W.; Cohen, M. L. *Nature* **1990**, *348*, 145–147. (b) Xiang, X.-D.; Zettl, A.; Vareka, W. A.; Corkill, J. L.; Barbee III, T. W.; Cohen, M. L. *Phys. Rev. B* **1991**, *43*, 11496–11499. (c) Choy, J.-H.; Kang, S.-G.; Kim, D.-H.; Hwang, S.-J.; Itoh, M.; Inaguma, Y.; Nakamura, T. *J. Solid State Chem.* **1993**, *102*, 284–287. (d) Muraoka, Y.; Kikuchi, M.; Nameki, H.; Awaji, S.; Suzuki, R.; Kobayashi, N.; Syono, Y. *Physica C* **1993**, *215*, 402–406.
- (19) (a) Pooke, D.; Kishio, K.; Kota, T.; Fukuda, Y.; Sandana, N.; Nagoshi, M.; Kitazawa, K.; Yamafuji, K. *Physica C* **1992**, *198*, 349–354. (b) Huang, T.; Itoh, M.; Yu, J.; Inaguma, Y.; Nakamura, T. *Phys. Rev. B* **1994**, *49*, 9885–9890.
- (20) (a) Xiang, X.-D.; Vareka, W. A.; Zettl, A.; Corkill, J. L.; Barbee III, T. W.; Cohen, M. L.; Kijima, N.; Gronsky, R.; *Science* **1991**, *254*, 1487–1489. (b) Xiang, X.-D.; Vareka, W. A.; Zettl, A.; Corkill, J. L.; Cohen, M. L. *Phys. Rev. Lett.* **1992**, *68*, 530–533. (c) Ma, J.; Alméras, P.; Kelley, R. J.; Berger, H.; Mararitondo, G.; Umezawa, A.; Cohen, M. L.; Onellion, M. *Physica C* **1994**, *227*, 371–376.
- (21) Park, N.-G.; Cho, S.-W.; Kim, S.-J.; Choy, J.-H. *Chem. Mater.* **1996**, *8*, 324–326.
- (22) Choy, J.-H.; Kim, D.-K.; Kang, S.-G.; Kim, D.-H.; Hwang, S.-J. In *Superconducting Materials*; Etourneau, J.; Torrance, J. B.; Yamauchi, H., Eds.; IIT-International: Paris, 1993; pp 329–334.
- (23) Because the iodine in the intercalated Ag–I layer interacts considerably with the BiO plane of host block, its scattering environment is quite different from $\beta\text{-AgI}$.
- (24) Gupta, P. *Phys. Rev. B* **1992**, *42*, 12767.
- (25) Lytle, F. W.; van der Laan, G.; Gregor, R. B.; Larson, E. M.; Violet, C. E.; Wong, J. *Phys. Rev. B* **1990**, *41*, 8955–8963.
- (26) Choy, J.-H.; Kim, D.-K.; Hwang, S.-H.; Demazeau, G. *Phys. Rev. B* **1994**, *50*, 16631–16639.
- (27) Yvon, K.; Francois, M. Z. *Phys. B* **1989**, *76*, 413–444.
- (28) Choy, J.-H.; Kim, D.-K.; Hwang, S.-H.; Park, J.-C. *J. Am. Chem. Soc.* **1995**, *117*, 7556–7557.
- (29) Manthiram, A.; Tang, X. X.; Goodenough, J. B. *Phys. Rev. B* **1990**, *42*, 138–149.
- (30) We could not perform reasonable fitting analyses for the pristine $\text{Bi}_2\text{Bi}_2\text{O}_{11}$ and its intercalates because of their complex crystal structures as well as the poor signal-to-noise (SN) ratio of their experimental spectra.
- (31) (a) Koizumi, A.; Maruyama, H.; Yamazaki, H.; Maeda, H.; Ishii, T.; Miura, Y.; Takada, J. *Physica C* **1992**, *190*, 338–344. (b) Lottici, P. P.; Antonoli, G.; Licci, F. *Physica C* **1988**, *152*, 468–474. (c) DiMarzio, D.; Wiesmann, H.; Chen, D. H.; Heald, S. M. *Phys. Rev. B* **1990**, *42*, 294–300.
- (32) In the fitting procedure, the bond distance and the Debye–Waller factor were allowed to be refined, whereas the coordination number was fixed to a crystallographic value due to the inaccuracies caused by its strong correlation with the Debye–Waller factor.
- (33) A decrease in (Cu–O_{st}) bond distance allows us to explain the aforementioned change of the peak A in XANES spectra upon intercalation; the shorter axial (Cu–O_{st}) bond reduces the effective LMCT along the c -axis by enhancing the electrostatic repulsion between the $4p_\pi$ electron and axial oxygen ligand, and therefore, the peak A corresponding to the $1s \rightarrow 4p_\pi$ transition with shakedown process is shifted toward a high-energy side.
- (34) Whangbo, M.-H.; Kang, D.-B.; Toradi, C. C. *Physica C* **1989**, *158*, 371–376.
- (35) (a) Shimakawa, Y.; Kubo, Y.; Manako, T.; Igarashi, H.; Izumi, F.; Asano, H. *Phys. Rev. B* **1990**, *42*, 10165–10171. (b) Martin, C.; Maignan, A.; Labbe, Ph.; Charadon, J.; Hejtmanek, J.; Raveau, B. *Chem. Mater.* **1995**, *7*, 1414. (c) Sequeira, A. A.; Yakhmi, J. V. *Studies of High-Temperature Superconductors*; Nova Science Publishers: New York; Vol. 11, 1993; pp 107–129.
- (36) Studer, F.; Bourgault, D.; Martin, C.; Retoux, R.; Michael, C.; Raveau, B.; Dartyge, E.; Fontaine, A. *Physica C* **1989**, *159*, 609–615.
- (37) Retoux, R.; Studer, F.; Michael, C.; Raveau, B.; Fontaine, A.; Dartyge, E. *Phys. Rev. B* **1990**, *41*, 193–199.
- (38) Choy, J.-H.; Kim, D.-K.; Demazeau, G.; Jung, D.-Y. *J. Phys. Chem.* **1994**, *98*, 6258–6262.
- (39) Choy, J.-H.; Kim, D.-K.; Hwang, S.-H.; Demazeau, G.; Jung, D.-Y. *J. Am. Chem. Soc.* **1995**, *117*, 8557–8566.
- (40) Choy, J.-H.; Kim, D.-K.; Park, N.-G.; Kim, D.-H.; Hwang, S.-J.; Hwang, S.-H.; Hur, N.-H. *Physica C* **1994**, *235–240*, 1023–1024.
- (41) (a) Huang, P. V.; Verma, A. L. *Phys. Rev. B* **1993**, *48*, 9869. (b) Trodahl, H. J.; Pooke, D.; Gainsford, G. J. Kishio, K. *Physica C* **1994**, *213*, 427–432.
- (42) In the $\text{IBi}_2\text{Bi}_2\text{O}_{11}$ sample used for preparing the Ag–I intercalate, the T_c decrease upon intercalation is determined to be 7 K.
- (43) Turbandt, C.; Lorenz, E. Z. *Phys. Chem.* **1913**, *87*, 513–542.
- (44) (a) Lidiard, A. B. In *Encyclopedia of Physics*; Flügge, S., Ed.; Springer-Verlag: Berlin, 1957; pp 258–260. (b) West, A. R. *Solid State Chemistry and Its Applications*; John Wiley & Sons Ltd: New York, 1984; p 453.
- (45) (a) Rice, M. J.; Roth, W. L. *J. Solid State Chem.* **1972**, *4*, 294–310. (b) Armstrong, R. D.; Bulmer, R. S.; Dickinson, T. *J. Solid State Chem.* **1973**, *8*, 219–228.
- (46) (a) Owens, B. B.; Argue, G. R. *Science* **1967**, *157*, 308–310. (b) Geller, S. *Science* **1967**, *157*, 310–312.

- (47) (a) Geller, S. *Science* **1972**, 176, 1016–1019. (b) Geller, S.; Skarstad, P. M. *Phys. Rev. Lett.* **1974**, 33, 1484–1486. (c) Geller, S.; Skarstad, P. M.; Wilber, S. A. *J. Electrochem. Soc.* **1975**, 122, 332–338. (d) Geller, S.; Lind, M. *J. Chem. Phys.* **1970**, 52, 5854–5861. (e) Chan, L. Y. Y.; Geller, S. *J. Solid. State. Chem.* **1977**, 21, 331–347.
- (48) Browall, K. K.; Kasper, J. S. *J. Solid State Chem.* **1975**, 15, 54.
- (49) Wittingham, M. S.; Huggins, R. A. *J. Electrochem. Soc.* **1971**, 118, 1–6.
- (50) Geller, S. In ref 3, p 55.
- (51) Such a peak splitting is attributed to the Ramsauer–Townsend resonance which occurs generally in the backscattering amplitude of a heavy element with a high atomic number.
- (52) Wells, A. F. *Structural Inorganic Chemistry*; Clarendon Press: Oxford, 1984; pp 410–411.
- (53) Boyce, J. B.; Hayes, T. M.; Stutius, W.; Mikkelsen, Jr, J. C. *Phys. Rev. Lett.* **1977**, 38, 1362–1365.
- (54) Choy, J.-H.; Yoon, J.-B.; Kim, D.-K.; Hwang, S.-H. *Inorg. Chem.* **1995**, 34, 6524–6531.
- (55) The magnitude of structure factor, $|F_{00l}|$, is the square root of the corrected intensity, I_{00l}/Lp , where I_{00l} and Lp are the observed intensity and Lorentz polarization factor, respectively. Because the sign of the structure factor is subject mainly to the z -coordinates of heavy ions in the $\text{Bi}_2\text{Sr}_2\text{Ca}_{n-1}\text{Cu}_n\text{O}_y$ lattice, the phase problem can be solved by assuming the retention of internal structure of host blocks during intercalation.
- (56) (a) Cava, R. J.; Reidinger, F.; Wuensch, B. J. *Solid State Commun.* **1977**, 24, 411–416. (b) Helmholz, L. *J. Chem. Phys.* **1935**, 3, 740–747.